Science Bulletin xxx (xxxx) xxx

Contents lists available at ScienceDirect

Science Bulletin

journal homepage: www.elsevier.com/locate/scib

Article

Decoupling Li-ion conduction and solvation structure in deep eutectic electrolytes for high-voltage lithium-ion batteries

Shida Xue [a,1], Xiangming Yao [a,1], Zhikang Deng [a,b,1], Jianjun Fang [a], Yingkang Liu [c], Yuxiang Huang [b], Xiaohu Wang [a], Guobiao Jin [a], Zhaohuang Zhan [a], Hongkai Yang [a], Zijin Xu [a], Zu-Wei Yin [d], Luyi Yang [a,*], Feng Pan [a,*]

[a] School of Advanced Materials, Peking University Shenzhen Graduate School, Shenzhen 518055, China
[b] Department of Chemistry, The University of Hong Kong, Hong Kong 999077, China
[c] School of Metallurgy and Environment, Central South University, Changsha 410083, China
[d] College of Energy, Xiamen University, Xiamen 361005, China

ARTICLE INFO

Article history:
Received 29 May 2025
Received in revised form 15 July 2025
Accepted 1 August 2025
Available online xxxx

Keywords:
Quasi-solid electrolytes
Deep eutectic electrolytes
Dimethyl sulfone
Li-ion conduction
Interfacial stability

ABSTRACT

As a promising deep eutectic quasi-solid electrolyte (DES) for Li-ion batteries, the application of dimethyl sulfone (DMS) is limited by its stability at the electrode–electrolyte interface. A common strategy to address this issue involves introducing additional anions into the Li-ion (Li^+) solvation sheath to stabilize the interphase. However, this approach often comes at the expense of ionic conductivity, which can negatively impact battery performance. In this work, a strategy to decouple Li^+ conduction and coordination structure is proposed. The introduction of lithium difluoroxalate borate (LiDFOB) promotes an anion-rich Li^+ solvation sheath, which facilitates the formation of stable interphases. More importantly, the incorporation of polyvinylidene fluoride (PVDF) frameworks regulates localized coordination structures and constructs fast Li^+ transport channels, liberating the movement of Li^+ from the constraints of their sluggish solvation clusters. As a result, this hierarchical regulation strategy not only achieves improved ionic conductivity, enabling high-rate operation, but also ensures the formation of stable interphases on 4.6 V $LiCoO_2$ cathode and graphite anode, exhibiting exceptional high-voltage operation stability for DESs. This work presents a promising approach to addressing critical challenges of DESs by achieving a balance between conductivity and interfacial stability, providing significant insights for their practical application.

1. Introduction

Solid-state batteries have gained significant attention in recent years as promising candidates for next-generation energy storage devices due to their enhanced safety, energy density, and cycling stability compared to conventional liquid electrolyte-based batteries [1]. However, solid electrolytes face challenges, such as limited ionic conductivity at room temperature and poor interfacial stability with electrodes, which hinder their practical application. Quasi-solid electrolytes (QSEs), on the other hand, offer a balanced solution by combining the high ionic conductivity of liquid electrolytes with the enhanced safety of solid electrolytes [2,3]. However, most existing QSEs are primarily based on polymer matrices. While polymer-based solid electrolytes such as polyvinylidene fluoride (PVDF) and polyacrylonitrile have been widely explored due to their mechanical stability and processability, they typically suffer from low room-temperature ionic conductivity and poor interfacial wettability with electrodes. These limitations often result in high interfacial resistance and sluggish Li^+ transport under practical conditions [4–9]. Compared to conventional polymer-based solid electrolytes, deep eutectic quasi-solid electrolyte (DES)-based QSEs typically offer higher room-temperature ionic conductivity, better interfacial wettability with electrodes, and simpler processing procedures, while still maintaining quasi-solid-state structural stability, making them an ideal compromise between liquid and solid-state systems [10–13]. These binary or ternary systems, formed by lithium salts and solid "solvents" through strong acid-base

* Corresponding authors.
E-mail addresses: yangly@pkusz.edu.cn (L. Yang), panfeng@pkusz.edu.cn (F. Pan).
[1] These authors contributed equally to this work.

https://doi.org/10.1016/j.scib.2025.08.004

interactions, offer numerous advantages, such as low cost, non-flammability, and high deformability, making them ideal candidates for solid-state batteries applications. Exhibiting high room-temperature ionic conductivity (exceeding 10^{-3} S cm^{-1}) and low costs, sulfone-based QSEs, such as dimethyl sulfone (DMS), have attracted wide attention [14]. However, the electrochemical window of DMS-based QSEs is not ideal, thus facing a series of interfacial issues in practical battery systems: not only does severe reduction decomposition occur at low working potentials, but oxidation decomposition also takes place at the cathode interface under high voltages.

To improve the interfacial stability of DMS-based QSEs, various attempts have been made. As one of the most promising approaches, the addition of lithium salt additives (such as lithium difluoroxalate borate (LiDFOB), lithium bis(oxalato)borate (LiBOB), etc.) not only facilitates the formation of desirable components in solid-electrolyte interphase (SEI) or cathode-electrolyte interphases (CEI), but also helps regulate the solvation structure of Li-ions (Li^+), forming contacted ion pairs (CIPs) or aggregates (AGGs), which aids in the decomposition of anions [15–18]. However, the increase in CIPs and AGGs often affects the ionic conductivity of the electrolyte, especially for QSEs, thereby sacrificing the rate performance of batteries [19].

In liquid electrolyte systems, local high-concentration electrolytes (LHCEs) are considered a hallmark strategy to address the above conflicting issues, as they can decouple ion transport from the solvation structure [20,21]. Drawing inspiration from the essence of LHCEs, we herein propose a hierarchical solvation structure modulation strategy in this work, which decouples ion conduction from its solvation structure (Scheme 1). On the one hand, the introduction of LiDFOB modulates the Li^+ solvation structure, leading to an anion-rich solvation sheath that induces stable interphases. On the other hand, the incorporation of PVDF frameworks induces localized solvation structure regulation, facilitating fast ion transport channels. This solvation structure regulation strategy allows the anions to be more effectively retained within the solvation shell of Li^+, thereby enabling the formation of stable interphases at the surface of the 4.6 V $LiCoO_2$ (LCO) cathode and the graphite (Gr) anode, achieving stable cycling of the full cell. It is equally important that the regulated solvation structure causes the ion transport mechanism to shift from the Arrhenius model to the Vogel-Tammann-Fulcher (VTF) model below the melting point, leading to an increase in the ionic conductivity of the QSE at room temperature [22]. The hierarchical solvation structure modulation strategy successfully balanced the conductivity and interfacial stability in DMS-based QSEs, which holds profound guiding value for their practical application.

2. Materials and methods

2.1. Materials

N-methyl pyrrolidone, DMS, lithium bis(trifluoromethanesulphonyl)imide (LiTFSI), LiDFOB, 1,4-dioxane were purchased from Aladdin. PVDF (Mw = 300,000, kynar 761) came from Arkema. The $Li_{1.2}Ni_{0.13}Co_{0.13}Mn_{0.54}O_2$ (LLMO) and the LCO were kindly provided by Xiamen XTC New Energy Materials Co., Ltd. Glass fiber filter membrane was purchased from Whatman Co.

2.2. Preparation of glass fiber reinforced single salt composite solid electrolyte

Initially, the single salt gel electrolyte was prepared by stirring a mixture of LiTFSI and DMS at 60 °C for 24 h (with a molar ratio of 4:1 for DMS to LiTFSI). Subsequently, the prepared gel electrolyte was spin-coated onto the surface of a glass fiber membrane at 60 °C, followed by a 6-h annealing period at this temperature, allowing the gel electrolyte to fully penetrate the glass fiber membrane (all the above processes were conducted in a glovebox filled with argon gas).

2.3. Preparation of glass fiber reinforced double salt composite solid electrolyte

Similarly, the dual salt gel electrolyte was prepared by stirring a mixture of LiTFSI, LiDFOB, and DMS at 60 °C for 24 h (with a molar ratio of DMS:LiTFSI:LiDFOB as 4:0.8:0.2). Subsequently, the prepared gel electrolyte was spin-coated onto the surface of a glass fiber membrane at 60 °C, followed by a 6-h annealing period at this temperature, allowing the gel electrolyte to fully penetrate the glass fiber membrane (all the above processes were conducted in a glovebox filled with argon gas).

2.4. Preparation of PVDF frame enhanced double salt composite solid electrolyte

Firstly, 1 g PVDF was added to 14.28 g 1,4-dioxane, and the mixture was stirred at 60 °C for 24 h to allow PVDF to fully dissolve in the 1,4-dioxane. After that, the precursor solution was poured into a glass template. Initially, the solution was pre-frozen by liquid nitrogen (the distance between liquid nitrogen and membrane was about 1.5 cm), and then it was wholly transferred into a vacuum freeze dryer at –86 °C for 24 h. The as-prepared PVDF porous 3D frameworks were also reheated to remove residual solvent and stored in the glove box. Subsequently, the dual salt gel electrolyte was spin-coated onto the PVDF porous 3D framework at 60 °C, followed by a 6 h annealing period at this temperature to allow the gel electrolyte to fully penetrate the PVDF porous 3D framework, thereby obtaining the PVDF composite electrolyte (this process was also conducted in a glovebox filled with argon gas) [23].

3. Results and discussion

3.1. Hierarchically modulated coordination structure

The DMS SE is fabricated by the incorporation of LiTFSI as the main salt and DMS solid solvent. To maintain the highest ionic conductivity at solid state, n_{Li}:n_{DMS} = 1:4 is chosen for the study (Fig. S1 online). The resultant electrolyte with pristine Li coordination is denoted as PLC. The high ionic conductivity observed in the PLC electrolyte (n_{Li}:n_{DMS} = 1:4) originates from the intrinsic features of deep eutectic systems. At this composition, the components form a eutectic structure that suppresses crystallization and leads to a structurally homogeneous yet mechanically stable quasi-solid-state matrix. The well-organized salt–solvent interactions and moderate hydrogen bonding maintain dynamic ionic domains that facilitate Li^+ transport. Given the interfacial instability between the electrolyte and electrode, LiDFOB as a film-forming additive is introduced, resulting in an electrolyte with anion modulated Li coordination structure (denoted as AMLC). In addition, PVDF, which preferentially interacts with a specific solvent in electrolyte, is selected as polymer backbone for additional solvation structure modulation [23]. The as-prepared QSE with hierarchically modulated Li^+ coordination is denoted as HMLC.

Differential scanning calorimetry (DSC) was performed to examine the thermal transitions of the DMS-based electrolytes. Pristine DMS exhibits a distinct melting peak at 116.28 °C, confirming its crystalline nature. In contrast, HMLC shows a lower glass transition temperature (T_g) than AMLC, which is attributed to specific interactions between the PVDF matrix and DMS molecules

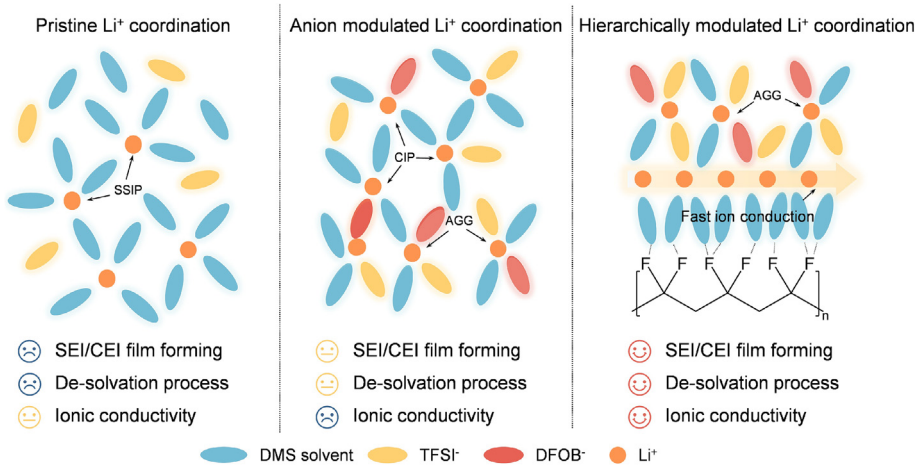

Scheme 1. Schematic diagram of Li^+ solvation structure regulation mechanism.

(Fig. S2 online). To assess the thermal stability of the quasi-solid-state electrolyte, thermogravimetric analysis (TGA) was performed on DMS, PLC, AMLC, and HMLC. The results indicate that HMLC exhibits the highest thermal stability among the tested electrolytes, as evidenced by its higher decomposition onset temperature and greater residual mass at elevated temperatures (Fig. S3 online).

Next, the fourier transform infrared (FTIR), the raman spectroscopy and the nuclear magnetic resonance (NMR) were employed to investigate the solvating coordination in the electrolytes. The FTIR spectra (Fig. 1a) exhibit an absorption peak within 750–730 cm^{-1}, which corresponds to the -SNS- stretching vibration of $TFSI^-$ anions [24]. In PLC, a higher proportion of solvent separated ion pairs (SSIPs) is observed, while the corresponding peak in the AMLC exhibits a blueshift to higher wavenumbers, indicating an increase in CIPs and AGGs. This blueshift is even more pronounced in the HMLC, suggesting a further increase in the proportion of CIPs and AGGs. For the free DMS solvent, the C-S-C symmetric stretching vibration is located at 760.9 cm^{-1} [25,26]. However, after the addition of LiTFSI, the corresponding peak in the PLC sample shifts to 764.8 cm^{-1}, indicating a stronger coordination between DMS and Li^+. Compared to PLC, the DMS absorption peaks in the AMLC and HMLC samples show a continuous redshift toward lower wavenumbers, indicating weakened coordination between DMS and Li^+. This results in more free solvent molecules, which indirectly suggests that Li^+ exhibits stronger Coulombic interactions with anions due to reduced solvent participation in coordination. Similar conclusions can be drawn from the Raman spectra of both DMS (Fig. 1b) and LiDFOB (Fig. S4 online), confirming the evolutions in the solvation environment of the electrolyte. Similar changes can be found in Li^+-$DFOB^-$ ion pairing. The hierarchically modulated solvation structure is further explored by NMR. PLC exhibits the highest value of ^7Li chemical shift, followed by AMLC, while HMLC has the lowest value (Fig. 1c) [27]. The continuous upfield shift results from a stronger shielding effect that implies enhanced Li^+-anion coordination. To reveal the intrinsic Li^+ coordination environments in the QSEs, density functional theory (DFT) and molecular dynamics (MD) theoretical calculations are employed [28]. The radial distribution function (RDF) analysis of PLC (Fig. 1d) shows that the initial RDF peaks of Li^+-O ($TFSI^-$) and Li^+-O (DMS) locate around 2.06 and 2.05 Å respectively. In the case of AMLC, the first solvation sheath exhibits a reduced solvent content and newly involved $DFOB^-$ anion, as indicated by the Li^+-O ($DFOB^-$) peak at 2.01 Å (Fig. 1e). In HMLC, the modulation effect of PVDF on the solvation sheath is confirmed by the further increase in anions and a reduced solvent proportion (Fig. 1f). The above findings demonstrate that LiDFOB and PVDF collaboratively participate in the regulation of solvation.

To probe the interaction between DMS and PVDF, electrostatic potentials (ESPs) were calculated (Fig. S5 online). The electron poor $-CH_3$ in DMS attracts the electron-rich –F group in PVDF through a dipole–dipole interaction, while the electron-rich =O group in DMS interacts with the electron-poor –H group in PVDF, resulting in the strong affinity between DMS and PVDF. In addition, the FTIR spectra (Fig. 1g) show that the absorption peak at 932 cm^{-1} assigned to free solvents is replaced by the coordinated DMS in PLC and AMLC. However, free and coordinated solvents coexist in HMLC due to the presence of PVDF, which causes DMS to move away from the solvation sheath owing to the affinity between DMS and PVDF. This mechanism is further verified by the intensified $-CH_3$ peak belonging to DMS in HMLC (Fig. 1h). Such favorable coordination is confirmed by the notably higher binding energy between PVDF and DMS compared to the commonly used glass fiber separator due to their low porosity and limited wettability with the electrolyte (Fig. S6 online). The aforementioned analysis demonstrates that the solvation structure of HMLC is synergistically regulated by both $DFOB^-$ anion and PVDF. Consequently, a solvation sheath containing more anions is achieved, effectively leading to a lower Li^+ de-solvation energy (Fig. 2i). This reduction in de-solvation energy facilitates faster ion migration, thereby improving the rate performance [29–32].

3.2. Decoupling of solvation structure and ion transport in HMLC

According to previous studies, an anion-rich solvation sheath tends to limit ion transport due to stronger ion-pairing [19,33,34]. This trade-off is clearly reflected in the Arrhenius plots (Fig. 2a), where the anion-rich solvation structure in AMLC restricts its ionic conductivity compared with PLC, especially in the Arrhenius region. Moreover, in both PLC and AMLC, ion transport shows a combination of Arrhenius behavior at low temperatures (25–50 °C) and VTF behavior at high temperatures (50–90 °C) [35,36]. HMLC exclusively follows VTF behavior, where Li^+ prefers vehicular-solvent coordinated motion. In this case, the ionic transport no longer depends on the sluggish DMS movement under lower temperatures, hence the improved ionic conductivity. This decoupling of solvation structure and ion transport is further supported by the significantly higher Li^+ transference number (t_{Li+}) in HMLC (0.75) compared to PLC and AMLC (Fig. 2b). Therefore, although HMLC features increased anion coordination, its hierar-

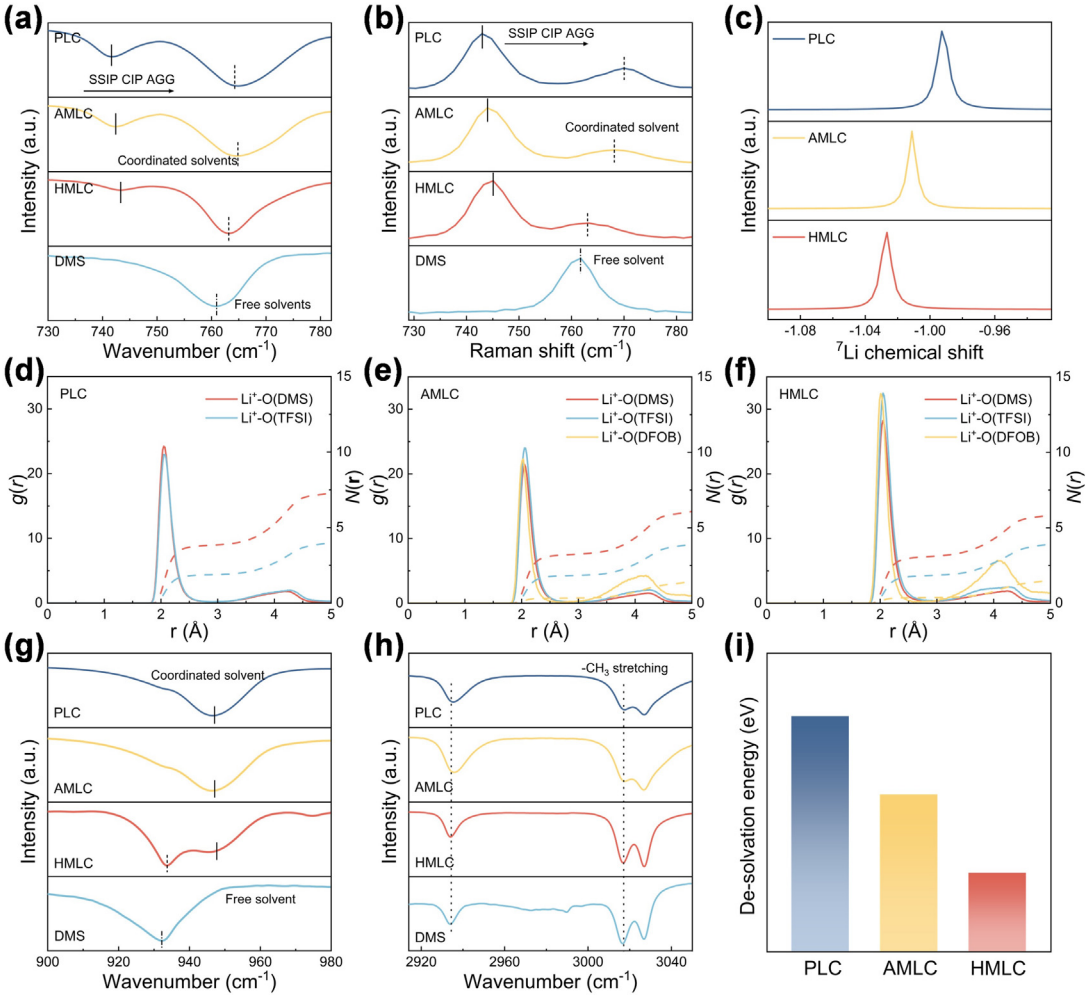

Fig. 1. (a) FTIR spectra of different electrolytes at the range of 730–780 cm^{-1}; (b) Raman spectra of different electrolytes at the range of 730–780 cm^{-1}; (c) NMR results of different electrolytes; (d–f) RDF and N(r) of PLC, AMLC, and HMLC, respectively; (g, h) FTIR spectra in different electrolytes at the range of 900–980 cm^{-1} and 2915–3050 cm^{-1}, respectively; (i) Calculated de-solvation energy in different electrolytes.

chical solvation structure facilitates efficient Li^+ transport through VTF-type pathways. This mitigates the common trade-off between ion aggregation and ionic mobility.

Next, we analyzed the diffusion coefficients of Li^+ (D_{Li}^+) through mean square displacement (MSD) calculations, where D is proportional to the slope of the time-dependent curves (Fig. 2c). The calculated D_{Li+} in the bulk electrolytes and at the PVDF/electrolyte interface (HMLC-interface) shows that, although HMLC-bulk exhibits a slightly lower D_{Li+} than AMLC and PLC, the highest D_{Li+} is observed at the HMLC interface, consistent with the improved ionic conductivity. The strong dipole–dipole interaction between DMS and PVDF induces solvent enrichment at the AMLC/PVDF interface, enabling rapid ion transfer through this solvent layer. Next, COMSOL numerical analysis of the current distribution in different SEs was carried out to visualize the Li^+ diffusion process. As shown in Fig. 2d–f, the change in color from blue to red represents the increase in electric potential. It is evident that HMLC exhibits the most uniform potential distribution due to rapid ion conduction, while the least uniformity is observed in AMLC. The ion transport under such confined regions means that the Li^+ conduction is no longer solely limited by the physico-chemical properties of DMS itself, allowing for the display of the VTF transport mode over a wider temperature range. Therefore, by decoupling ion transport and solvation structure in HMLC, the increased ion pairs in the solvation sheath contribute to the SEI/CEI formation, while Li^+ can freely transport along the DMS/PVDF interface.

3.3. In-situ characterization of interfacial evolution

In-situ FTIR was used to investigate the electrolyte decomposition behaviors during CEI/SEI formation in various electrolytes [37]. For the LCO cathode, as the voltage increased from open circuit voltage (OCV) to 4.6 V, severe solvent decomposition could be observed in PLC, evidenced by the pronounced reverse peaks of DMS (~741 cm^{-1}) and Li^+-DMS (~766 cm^{-1}), signifying extensive solvent breakdown. In contrast, AMLC and HMLC electrolytes exhibited much less solvent decomposition, with HMLC showing the most effective suppression of solvent degradation (Fig. 3a–c). It can be speculated that the anion-rich Li^+ coordination environments lead to the formation of anion-derived CEI, which stabilizes the interface and prevents uncontrolled electrolyte decomposition. This hypothesis is supported by the *in-situ* Raman spectra (Fig. S7 online), where the two characteristic peaks at 485 and 595 cm^{-1} can be assigned to the O-Co-O bending (E_g) and Co-O stretching (A_{1g}) of LCO, respectively. During charging, all cells showed similar trends. The peak intensity of E_g and A_{1g} tends to reduce, corresponding to the bond weakening due to de-lithiation. Upon charging, LCO with PLC exhibited dramatic attenuation in the E_g and A_{1g}

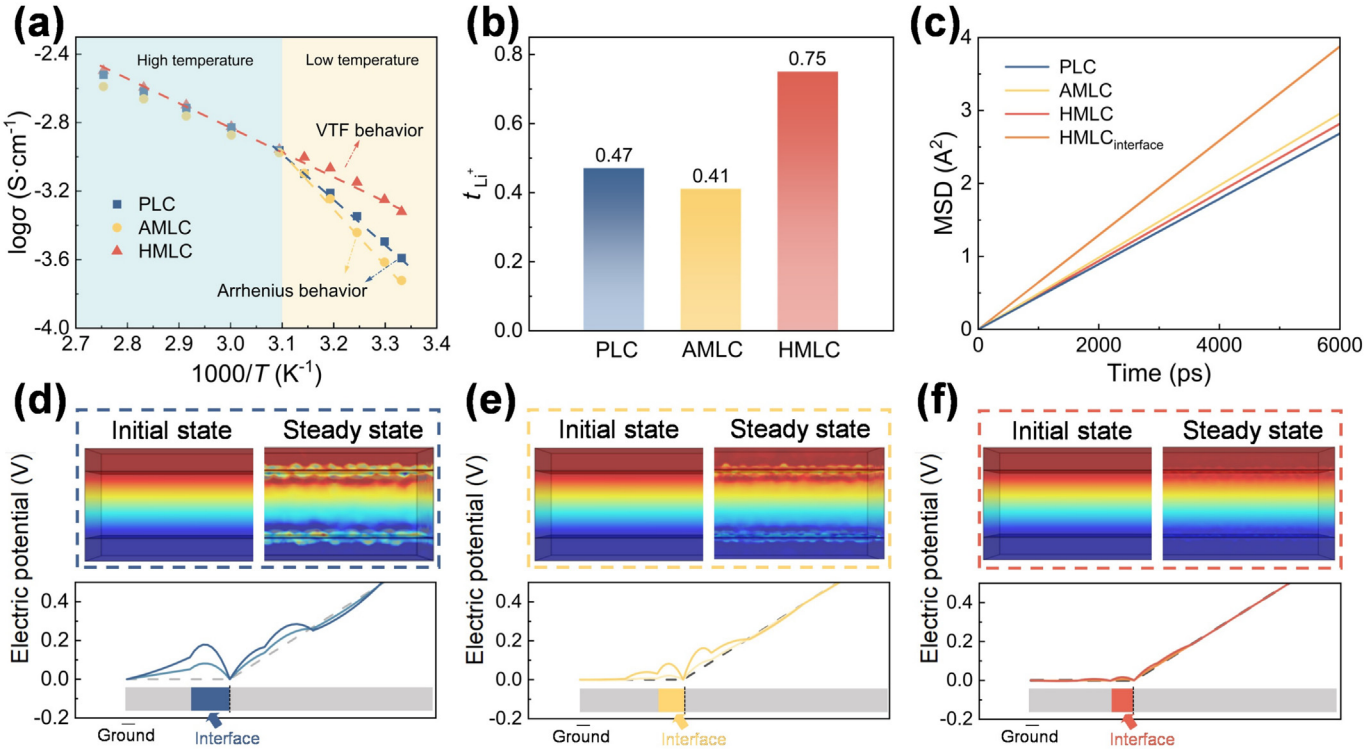

Fig. 2. (a) Ionic conductivities of different electrolytes. (b) Values of t_{Li+} of PLC and AMLC and HMLC. (c) Mean squared displacement (MSD) of Li^+ in different electrolytes. The current distribution in (d) PLC, (e) AMLC, and (f) HMLC electrolytes to visualize the Li^+ diffusion process.

peaks, resulting from the severe reaction on the LCO/PLC interface. As for AMLC, the two peaks have reemerged, but the recovery is insufficient. In comparison, HMLC exhibits the best reversibility during cycling due to the superior interfacial stability, which greatly prevents the irreversible breaking of Co-O and O-Co-O bonds on the surface, which could further prohibit the structural collapse of LCO [38].

Another issue that DMS faces in commercial applications is its extreme incompatibility with Gr anodes, as demonstrated in the cycling performance of Li||Gr half-cell with PLC (Fig. S8 online), which shows almost no capacity. During the discharge of the Gr anode from OCV to 0.01 V, extensive solvent decomposition took place in PLC, as evidenced by the significantly intensified DMS and Li^+-DMS reverse peaks. In contrast, reduced solvent peaks were observed in both AMLC and HMLC, with HMLC demonstrating a stronger inhibitory effect on DMS consumption (Fig. 3d–f). *In-situ* EIS further revealed that during the discharge process from OCV to 0.01 V, SEI formation begins at around 1.5 V for both AMLC and HMLC (Fig. S9 online), indicating earlier interphase formation; whereas for PLC, the SEI formation does not occur until 1.2 V. This earlier formation of the SEI layer in HMLC contributes to its better interfacial stability, as reflected in the significantly lower impedance of HMLC compared to AMLC and PLC. The early and stable SEI formation in HMLC helps to form a robust passivation layer that effectively prevents further electrolyte degradation, resulting in a superior electrochemical performance.

3.4. Improved electrical chemical performance

To evaluate the electrochemical performance of the as-prepared electrolytes, LCO||Li cells with different SEs are assembled and tested with a charge cut-off voltage at 4.6 V. Long-term cycling results (Fig. 4a) show that with an initial discharge capacity of 193 mAh g^{-1} and a high-capacity retention of 93.1% after 200 cycles at 0.2 C, HMLC delivers a superior cycling performance over PLC (failed after 100 cycles) and AMLC (capacity retention of 45.5% at 200 cycles), the high-voltage cycling performance of HMLC surpasses most previous reports (Fig. S10 and Table S1 online). *Ex-situ* Raman spectra revealed that after cycling, electrodes using AMLC and PLC electrolytes showed an increase in spinel Co_3O_4 components, while the formation of such electrochemically inactive phase was effectively suppressed in HMLC (Fig. S11 online), hence the enhanced cycling stability [39]. Furthermore, transmission electron microscopy (TEM) images (Fig. S12 online) confirmed the formation of spinel phase at the near-surface region of the LCO cycled in PLC and AMLC, while layered structure remains intact for HMLC.

The corresponding charge–discharge profiles of HMLC (Fig. 4b) exhibit lower overpotential than PLC (Fig. S13a online) and AMLC (Fig. S13b online). This tendency is also found in the cyclic voltammetry (CV) curves (Fig. S14 online), indicating the favorable kinetic process facilitated by HMLC. The improved cycling stability by HMLC is also demonstrated at a higher rate of 0.5 C (Fig. S15 online). Benefiting from the improved Li-conduction and modulated solvation structure, HMLC displays superior rate capability over other electrolytes (Fig. 4d). Linear sweep voltammetry (LSV) measurements (Fig. S16 online) further confirm that HMLC exhibits the widest electrochemical stability window among the three electrolytes. To verify the universality of this electrolyte design strategy, LLMO is paired with different DMS-based electrolytes and tested under 0.5 C. As a result, HMLC delivered a higher capacity retention of 86.6% over 200 cycles, outperforming AMLC and PLC (Fig. S17 online). The enhanced interfacial stability at high-voltage and rate performance demonstrated by HMLC can be attributed to its optimized solvation structure.

As an important parameter to evaluate the stability towards Li dendrite growth, the maximum current density is tested for different electrolytes by performing galvanostatic cycling for Li||Li sym-

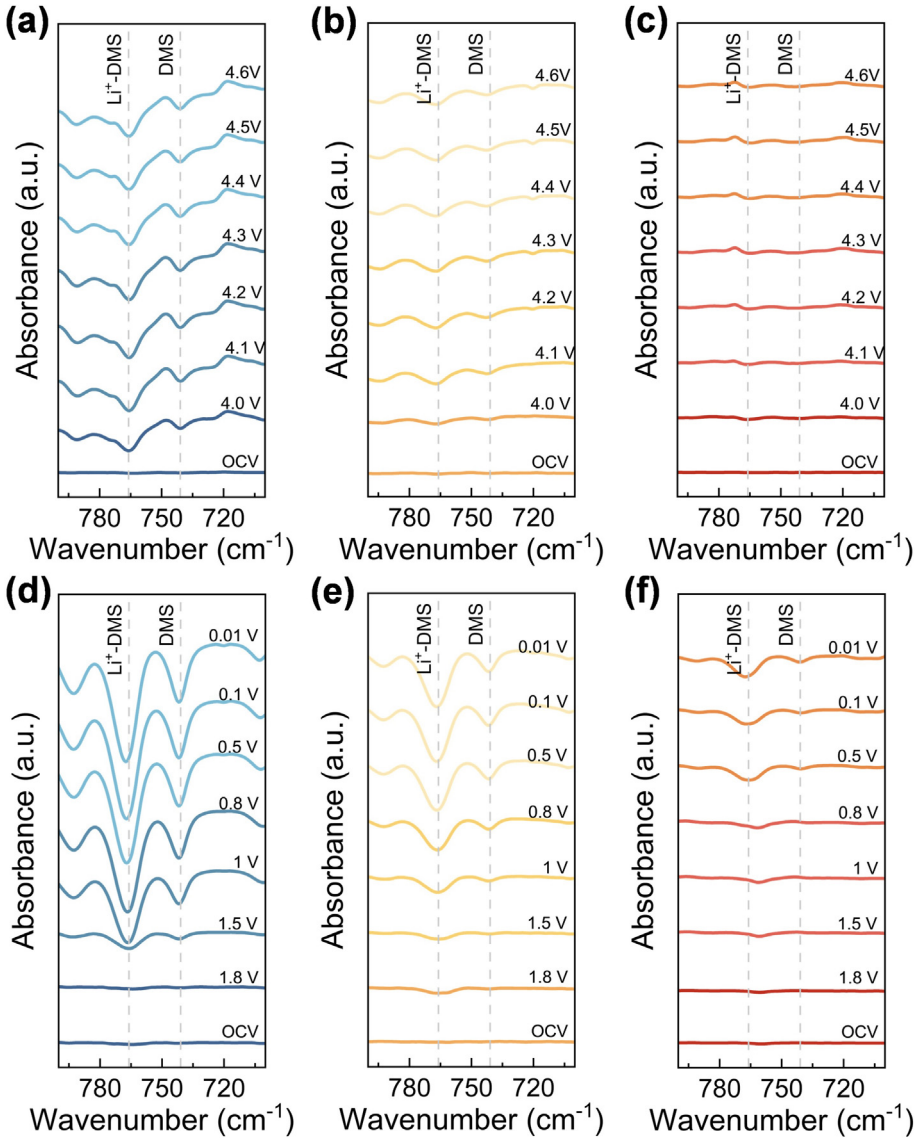

Fig. 3. *In-situ* FTIR difference spectra on LCO cathode surface during galvanostatic charging to 4.6 V with PLC (a), AMLC (b), and HMLC (c) electrolytes; *In-situ* FTIR difference spectra on Gr anode surface during galvanostatic discharging to 0.01 V with PLC (d), AMLC (e), and HMLC (f) electrolytes.

metric cells with an increasing current density (Fig. S18 online). It is shown that the stable cycling with low polarization for HMLC is achieved with a current density as high as 0.8 mA cm^{-2}, outperforming PLC (short-circuited at 0.4 mA cm^{-2}) and AMLC (short-circuited at 0.6 mA cm^{-2}). The voltage profiles (Fig. S19 online) during long-term Li plating/stripping process are recorded at 25 °C with a current density of 0.2 mA cm^{-2}. The poor cycling performance of Li||Li cell with PLC implies the intrinsic instability between DMS and Li metal. As for AMLC, the assembled cell shows stable cycling up to 1100 h, followed by a gradual increase in polarization and a short circuit after 2200 h. In contrast, HMLC is able to maintain stable cycling for more than 3500 h, and is accompanied by a much smaller polarization voltage.

Benefiting from the regulated Li solvation sheath, Gr anode is compatible with both AMLC and HMLC (Fig. 4c and Fig. S20 online): HMLC displays exceptional cyclic stability under 0.5 C, retaining 94.9% of its capacity after 150 cycles, while AMLC encounters capacity decay after 100 cycles. Temperature-dependent EIS was further employed to evaluate the kinetics of different interfacial processes. The activation energy of Li de-solvation (E_{a1}) in HMLC (44.1 kJ mol^{-1}) is calculated to be significantly lower than that of PLC (73.2 kJ mol^{-1}) and AMLC (64.1 kJ mol^{-1}), indicating a facile de-solvation process (Fig. S21 online). Therefore, it can be inferred that HMLC, due to its anion-enriched lithium-ion solvation sheath, avoids solvent co-intercalation that can lead to Gr structural damage, thus achieving excellent interfacial stability with Gr.

To further demonstrate the potential of HMLC for practical application, LCO||Gr full cells were assembled and tested. In coin cells, HMLC enabled a satisfactory cyclic performance during 200 cycles, with a high-capacity retention of 91.5% under 1 C (Fig. 4e). Based on EIS results, the cell using HMLC exhibited much lower impedance values than those with other electrolytes after cycling (Fig. S22 online), suggesting that the failure in bulk LCO and Gr originates from the surface. Furthermore, solid-state pouch cells are assembled and tested (Fig. S23 online). The flexible pouch cells were able to reliably power a light-emitting diode without short-circuiting during bending, cutting and igniting tests, and also successfully passed the nail penetration test, demonstrating superior safety of HMLC (Fig. 4f and Fig. S24 online). Finally, an 11 V

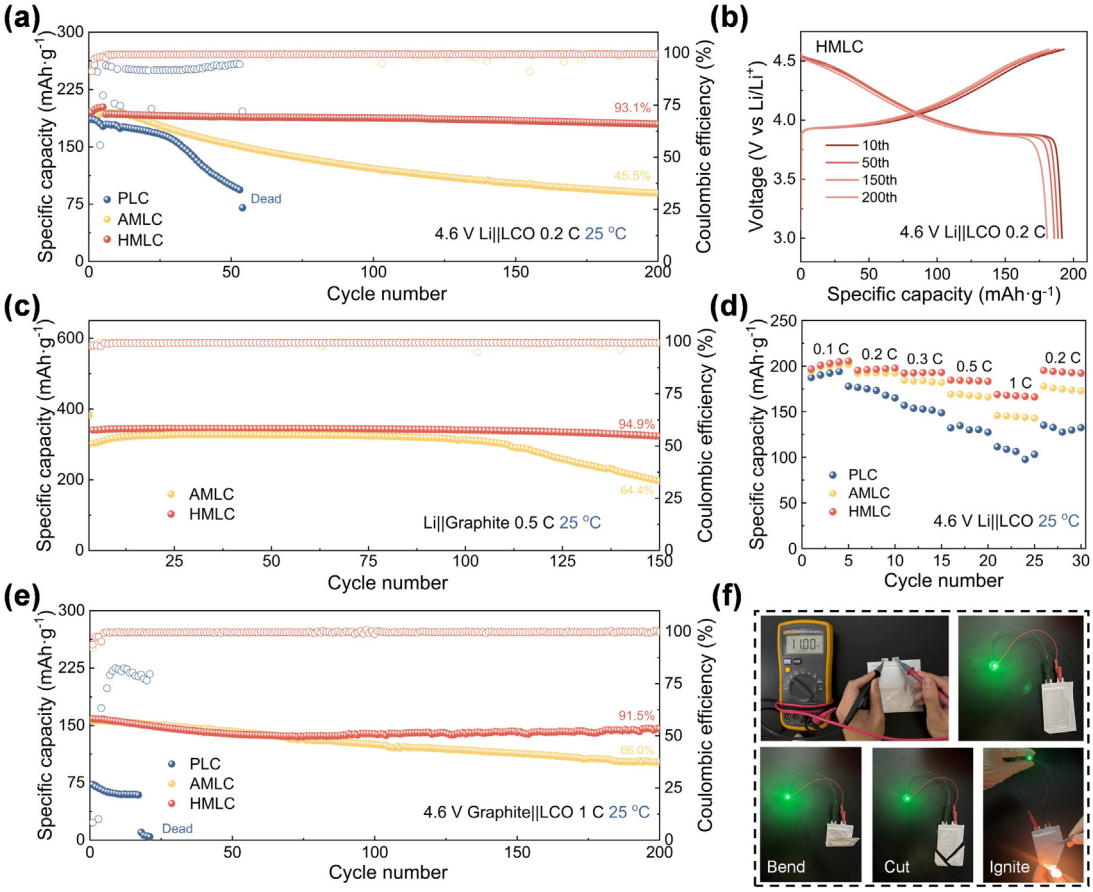

Fig. 4. (a) Galvanostatic cycling performance and Coulombic efficiency of Li||LCO cells with various electrolytes at a current density of 0.1 C for the first 5 cycles and 0.2 C for subsequent cycles at 25 °C. (b) Charge–discharge profiles of LCO cathodes with HMLC in the voltage range of 3.0–4.6 V. (c) Galvanostatic cycling performance and Coulombic efficiency of Li||Gr cells with various electrolytes at a current density of 0.1 C for the first 5 cycles and 0.5 C for subsequent cycles at 25 °C. (d) Charge–discharge profiles of Gr anodes with HMLC in the voltage range of 0.01–1 V. (e) Galvanostatic cycling performance and Coulombic efficiency of LCO||Gr pouch cells at a rate of 0.2 C using HMLC. (f) Pouch cell usability test.

pouch cell with a direct internal connection was successfully assembled, showcasing the potential for achieving high-energy-density batteries.

3.5. Characterizations of SEI and CEI

From the above, it can be concluded that the differences in electrochemical performance arise from variations in interfacial stability, which is determined by the SEI or CEI. Therefore, we conducted a series of characterizations on the SEI and CEI. First, X-ray photoelectron spectroscopy (XPS) was used to characterize the compositional information of interphases on both electrodes of LCO||Gr full cells after cycled. Compared with PLC, the modified solvation structures in AMLC and HMLC led to the formation of a CEI film containing LiF, B-O, and B-F bonds, which can be attributed to the decomposition of anions in AGGs (Fig. 5a and b). Due to the presence of B-O and B-F groups with strong electron-withdrawing effects, the CEI's antioxidant performance can be significantly enhanced [15]. At the same time, the substantial amount of LiF provides the CEI with good electronic insulation and mechanical strength [40]. For the Gr anodes cycled in different electrolytes (Fig. 5c and d), the F 1s and B 1s spectra demonstrated even more significant differences in the SEI composition. Compared to the CEI, the SEI formed with HMLC contains higher relative amounts of LiF and B-F containing compounds [41]. These components, which possess high mechanical strength and excellent electronic insulation properties, are more effective in passivating and protecting the Gr anode. Therefore, the superior compatibility between HMLC and Gr is attributed to the accelerated desolvation process and the construction of a robust SEI film, both of which stem from the hierarchically modified solvation structure.

To explore the interfacial stability of HMLC toward the electrodes, time-of-flight secondary ion mass spectroscopy (TOF-SIMS) was conducted to visualize the spatial distribution of various compositions in the as-formed CEI and SEI (Fig. 5e and f) of LCO||Gr full cell [42]. Both CEI and SEI formed in HMLC exhibit similar layered structures, which significantly enhances interfacial stability and electrochemical performance (Fig. 5g). The outer layer is enriched with BF_2^- derived from the LiDFOB additive. Due to the high thermal stability and density of compounds containing B-F bonds. They can form a stable and dense protective shell that inhibits direct contact between the electrolyte and the surface of the active material. Additionally, as mentioned earlier, their excellent antioxidant capability ensures the stability of the CEI under high voltage. Moreover, the inner layers of both CEI and SEI predominantly consist of LiF, which not only provides stable structural support for the interphases but also blocks electron transport due to its wide band gap. Therefore, the hierarchical modulation of the solvation structure in HMLC facilitates the formation of robust CEI and SEI with layered structures, ensuring superior stability during high-voltage cycling.

4. Conclusion

In this study, we proposed a novel hierarchical solvation structure modulation strategy to decouple the conduction of Li^+ from the solvation structure in a DMS-based QSE. On the one

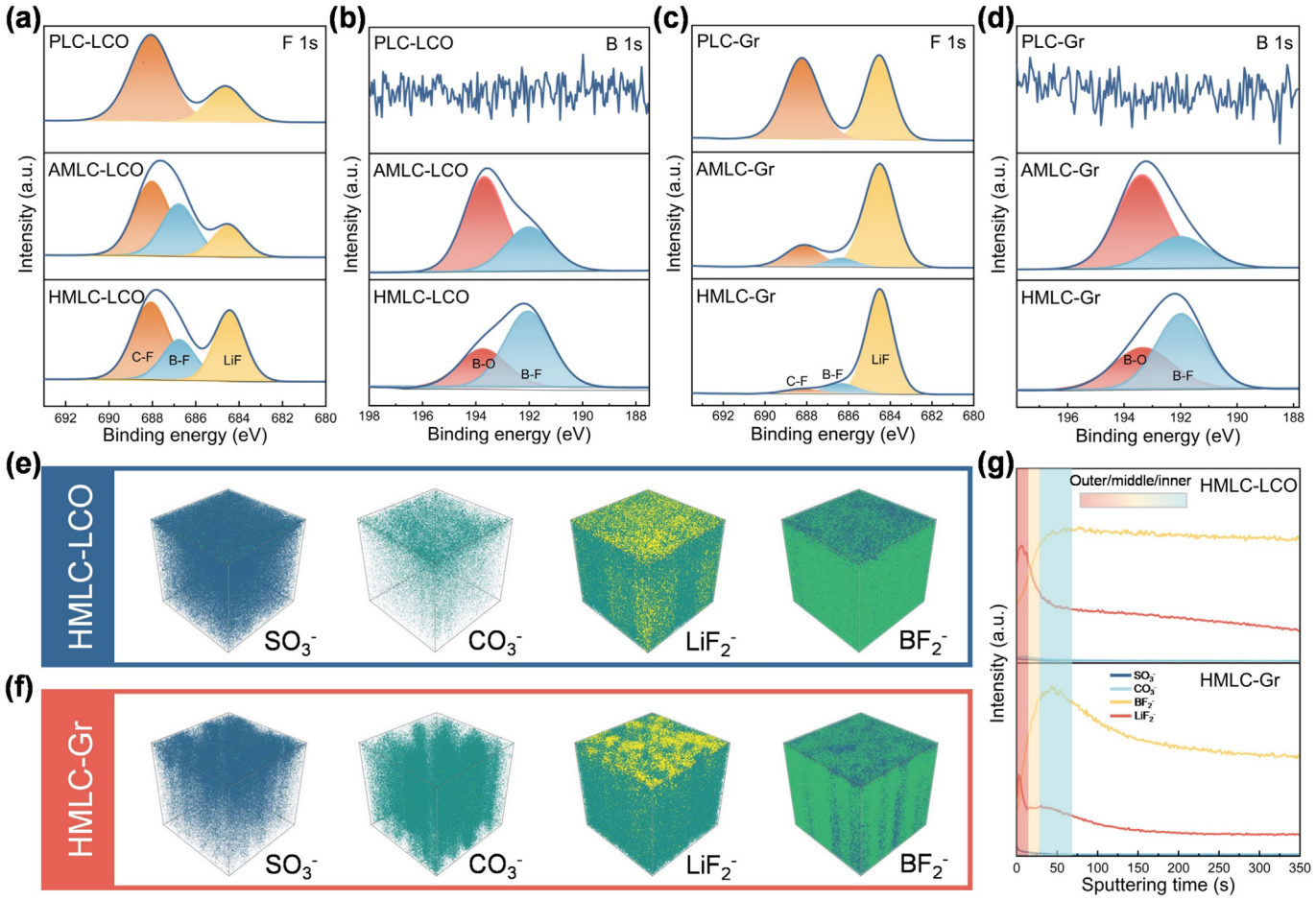

Fig. 5. F 1s (a), B 1s (b) XPS spectra of LCO cathodes with various electrolytes after 200 cycles; F 1s (c), B 1s (d) XPS spectra of Gr anodes with various electrolytes after 200 cycles; TOF-SIMS three-dimensional distributions on LCO cathodes with HMLC (e), and Gr anodes (f) with HMLC electrolytes after 200 cycles; Depth profiles of various secondary ion fragments during the TOF-SIMS measurement for LCO cathodes and Gr anodes (g).

hand, the introduction of LiDFOB as an additive led to an anion-rich solvation sheath, facilitating the formation of stable interphases at both the cathode and anode. On the other hand, the incorporation of PVDF frameworks regulated the solvation structure and created fast Li^+ transport channels, which liberated the movement of Li^+ from the constraints of their solvation clusters. As a result, the DMS-based QSEs exhibited improved electrochemical performance, with superior rate capability and long cycling stability, particularly when paired with the high-voltage LCO cathode and the Gr anode. By offering a balanced solution between conductivity and interfacial stability, this study presents a promising and practical approach to address the challenges associated with DESs. We acknowledge, however, that the current study primarily relies on indirect transport analysis to support the proposed decoupling mechanism. While these findings suggest the formation of alternative conduction pathways, more direct evidence—such as spatially resolved conductivity measurements or spectroscopic analysis-is needed to fully validate the interfacial transport process. Future research efforts should prioritize advanced techniques such as neutron reflectometry or NMR-based ion mobility mapping to further elucidate the underlying mechanisms.

Conflict of interest

The authors declare that they have no conflict of interest.

Acknowledgments

This work was supported by the Material Genome Big-Science Facilities Platform (supported by the Municipal Development and Reform Commission of Shenzhen), the International Joint Research Center for Electric Vehicle Power Battery and Materials (2015B01015), the Guangdong Key Laboratory of Design and Calculation of New Energy Materials (2017B030301013), the Shenzhen Key Laboratory of New Energy Resources Genome Preparation and Testing (ZDSYS201707281026184), and the Shanghai Synchrotron Radiation Facility (SSRF, beamline 02B02).

Author contributions

Shida Xue, Xiangming Yao, Zhikang Deng, Luyi Yang, and Feng Pan conceived the idea and designed the experiments. Shida Xue synthesized all the materials and conducted electrochemical measurements. Xiangming Yao and Yingkang Liu conducted all calculations. Zhikang Deng conducted the *in-situ* FTIR. Jianjun Fang made the pouch cell. Yuxiang Huang performed the *in-situ* Raman and the NMR tests. Xiaohu Wang and Guobiao Jin conducted the XPS. Hongkai Yang and Zhaohuang Zhan conducted the TEM tests. Zijin Xu and Zuwei Yin performed the TOF-SIMS. Shida Xue, Xiangming Yao, Zhikang Deng, Luyi Yang, and Feng Pan wrote the manuscript and all authors edited the manuscript.

Appendix A. Supplementary material

Supplementary data to this article can be found online at https://doi.org/10.1016/j.scib.2025.08.004.

References

[1] Kim JG, Son B, Mukherjee S, et al. A review of lithium and non-lithium based solid state batteries. J Power Sources 2015;282:299–322.
[2] Liu FZ, Wang JY, Chen WY, et al. Polymer-ion interaction prompted quasi-solid electrolyte for room-temperature high-performance lithium-ion batteries. Adv Mater 2024;36:2409838.
[3] Wang QR, Xu HL, Fan YC, et al. Insight into multiple intermolecular coordination of composite solid electrolytes via cryo-electron microscopy for high-voltage all-solid-state lithium metal batteries. Adv Mater 2024;36:2314063.
[4] Deng ZK, Chen SM, Yang K, et al. Tailoring interfacial structures to regulate carrier transport in solid-state batteries. Adv Mater 2024;36:2407923.
[5] Yao XM, Chen SM, Wang CH, et al. Interface welding via thermal pulse sintering to enable 4.6 V solid-state batteries. Adv Energy Mater 2023;14:2303422.
[6] Tian WY, Li ZP, Miao LC, et al. Composite quasi-solid-state electrolytes with organic–inorganic interface engineering for fast ion transport in dendrite-free sodium metal batteries. Adv Mater 2024;36:2308586.
[7] Liu YX, Wang SQ, Chen WC, et al. 5.1 μm ion-regulated rigid quasi-solid electrolyte constructed by bridging fast Li-ion transfer channels for lithium metal batteries. Adv Mater 2024;36:2401837.
[8] Chang Z, Yang HJ, Zhu XY, et al. A stable quasi-solid electrolyte improves the safe operation of highly efficient lithium-metal pouch cells in harsh environments. Nat Commun 2022;13:1510.
[9] Zhu C, Chen SM, Li K, et al. Quantitative analysis of the structural evolution in Si anode via multi-scale image reconstruction. Sci Bull 2023;68:408–16.
[10] Prakash P, Fall B, Aguirre J, et al. A soft co-crystalline solid electrolyte for lithium-ion batteries. Nat Mater 2023;22:627–35.
[11] Zhou KX, Dai XK, Zhang L, et al. Enhancing stability and safety of commercial solid-state lithium batteries through ternary eutectic solvents for solid-state electrolyte interface modification. Adv Energy Mater 2024;15:2402782.
[12] Jaumaux P, Liu Q, Zhou D, et al. Deep-eutectic-solvent-based self-healing polymer electrolyte for safe and long-life lithium-metal batteries. Angew Chemie-Int Ed 2020;59:9134–42.
[13] Wu JX, Liang QH, Yu XL, et al. Deep eutectic solvents for boosting electrochemical energy storage and conversion: a review and perspective. Adv Funct Mater 2021;31:2011102.
[14] Xie YF, Xu LL, Tong Y, et al. Molten guest-mediated metal–organic frameworks featuring multi-modal supramolecular interaction sites for flame-retardant superionic conductor in all-solid-state batteries. Adv Mater 2024;36:2401284.
[15] Yang XR, Huang YX, Li JH, et al. Understanding of working mechanism of lithium difluoro(oxalato) borate in Li||NCM85 battery with enhanced cyclic stability. Energy Mater 2023;3:300029.
[16] Xiao A, Yang L, Lucht BL. Thermal reactions of $LiPF_6$ with added LiBOB. Electrochem Solid St 2007;10:241–4.
[17] Mao ML, Ji X, Wang QY, et al. Anion-enrichment interface enables high-voltage anode-free lithium metal batteries. Nat Commun 2023;14:1082.
[18] Ji YC, Huang YX, Dong ZH, et al. Anion adsorption at the inner-helmholtz plane directs cathode electrolyte interphase formation. Angew Chemie-Int Ed 2025;64:e20242553.
[19] Rampal N, Weitzner SE, Cho S, et al. Structural and transport properties of battery electrolytes at sub-zero temperatures. Energy Environ Sci 2024;17:7691–8.
[20] Song G, Yi ZL, Su FY, et al. Boosting the low-temperature performance for Li-ion batteries in $LiPF_6$-based local high-concentration electrolyte. ACS Energy Lett 2023;8:1336–43.
[21] Chen J, Zhang H, Fang MM, et al. Design of localized high-concentration electrolytes via donor number. ACS Energy Lett 2023;8:1723–34.
[22] Aziz SB, Woo TJ, Kadir MFZ, et al. A conceptual review on polymer electrolytes and ion transport models. J Sci: Adv Mater Devices 2018;3:1–17.
[23] Sun JQ, Yao XM, He CH, et al. Highly stable lithium batteries enabled by composite solid electrolyte with synergistically enhanced in-built ion-conductive framework. J Power Sources 2022;545:231928.
[24] Wei Y, Liu TH, Zhou W, et al. Enabling all-solid-state Li metal batteries operated at 30 °C by molecular regulation of polymer electrolyte. Adv Energy Mater 2023;13:2203547.
[25] Davies JED, Lie Ken Jie MSF, Bakare O. Raman studies of thia fatty acid esters. Chem Phys Lipids 1990;56:223–6.
[26] Uno T, Machida K, Hanai K. Vibrational spectra of dimethyl sulphone and dimethyl sulphone-d_6. Spectrochim Acta A: Mol Spectrosc 1971;27:107–18.
[27] Piao ZH, Ren HR, Lu GX, et al. Stable operation of lithium metal batteries with aggressive cathode chemistries at 4.9 V. Angew Chemie-Int Ed 2023;62:e202300966.
[28] Ji YP, Dong LW, Liu JP, et al. A Li^+-flux-homogenizing separator for long-term cycling of Li metal anodes. Energy Environ Sci 2024;17:4078–89.
[29] Kim SC, Gao X, Liao SL, et al. Solvation-property relationship of lithium-sulphur battery electrolytes. Nat Commun 2024;63:e202412214.
[30] Liang P, Hu H, Dong Y, et al. Competitive coordination of ternary anions enabling fast Li-ion desolvation for low-temperature lithium metal batteries. Adv Funct Mater 2024;34:2309858.
[31] Liu X, Zhang JW, Yun XY, et al. Anchored weakly-solvated electrolytes for high-voltage and low-temperature lithium-ion batteries. Angew Chemie-Int Ed 2024;63:e202406596.
[32] Wang YC, Ji YC, Yin ZW, et al. Tuning rate-limiting factors for graphite anodes in fast-charging Li-ion batteries. Adv Funct Mater 2024;63:e202412214.
[33] Xue S, Zhou Y, Zhang ZW, et al. "Dragging" effect induced formation of AGGs-rich solvation structures in lithium metal batteries. J Energy Storage 2024;95:112558.
[34] Deng RY, Chu FL, Kwofie FL, et al. A low-concentration electrolyte for high-voltage lithium-metal batteries: fluorinated solvation shell and low salt concentration effect. Angew Chemie-Int Ed 2022;61:e202215866.
[35] Tao RY, Miyamoto D, Aoki T, et al. Novel liquid lithium borates characterized with high lithium ion transference numbers. J Power Sources 2004;135:267–72.
[36] Das S, Ghosh A. Charge carrier relaxation in different plasticized PEO/PVDF-HFP blend solid polymer electrolytes. J Phys Chem B 2017;121:5422–32.
[37] Chen SM, Deng ZK, Li JX, et al. Tuning reaction kinetics of fluorinated molecules to construct robust solid electrolyte interphases on SiO_x anode. Angew Chemie-Int Ed 2025;64:e202413927.
[38] Zhang H, Huang YX, Wang Y, et al. *In-situ* constructed protective bilayer enabling stable cycling of $LiCoO_2$ cathode at high-voltage. Energy Storage Mater 2023;62:102951.
[39] Zheng GR, Xue SD, Li YH, et al. Anion-mediated interphase construction enabling high-voltage solid-state lithium metal batteries. Nano Energy 2024;125:109617.
[40] Zhou T, Wang JZ, Lv L, et al. Anion-π interaction and solvent dehydrogenation control enable high-voltage lithium-ion batteries. Energy Environ Sci 2024;17:9185–94.
[41] Xiao A, Yang L, Lucht BL, et al. Examining the solid electrolyte interphase on binder-free graphite electrodes. J Electrochem Soc 2009;156:A318.
[42] Yang K, Ma JB, Li YH, et al. Weak-interaction environment in a composite electrolyte enabling ultralong-cycling high-voltage solid-state lithium batteries. J Am Chem Soc 2024;146:11371–81.